Research Square

Preprints are preliminary reports that have not undergone peer review.
They should not be considered conclusive, used to inform clinical practice,
or referenced by the media as validated information.

An intra-host mathematical model for rabies infection with structured axonal transport and post-exposure control strategies

Hippolyte Djimramadji

hippolytedjimramadji@gmail.com

University of N'Djamena

Siguy Dawe

University of N'Djamena

Hisseine Bachar Mahamat

University of N'Djamena

Article

Keywords:

Posted Date: November 20th, 2026

DOI: https://doi.org/10.21203/rs.3.rs-11327433/v1

License: This work is licensed under a Creative Commons Attribution 4.0 International License.
Read Full License

Additional Declarations: No competing interests reported.

An intra-host mathematical model for rabies infection with structured axonal transport and post-exposure control strategies

Hippolyte Djimramadji*[1], Siguy Dawe[1], and Hisseine Bachar Mahamat[1]

[1]Department of Mathematics, University of N'Djamena, Chad
*hippolytedjimramadji@gmail.com

October 17, 2026

Abstract

We propose a novel intra-host mathematical model for rabies virus infection, which mechanistically integrates the main stages of viral progression from the inoculation site to the salivary glands. The model is formulated as a system of nonlinear ordinary differential equations coupling the dynamics of local muscle infection, nonlinear viral capture by peripheral nerve endings (modeled by a Hill function), structured retrograde axonal transport as a chain of successive compartments, central nervous system invasion, salivary dissemination, a local effector immune response, and three time-dependent post-exposure control strategies. A key novelty lies in the explicit representation of the neurotropic progression of the virus via discrete axonal steps, offering a suitable framework to study therapeutic windows and optimized interventions.

Mathematical analysis establishes the positivity and boundedness of solutions as well as the existence and uniqueness of a global solution. A disease-free equilibrium is identified, and a basic reproduction number $\mathcal{R}_0$ is derived, defining a threshold for local infection establishment. A local stability condition is stated, and a Lyapunov function is constructed to demonstrate the global asymptotic stability of the disease-free equilibrium when $\mathcal{R}_0 < 1$, valid for any Hill cooperativity $q \geq 1$. A mechanistic neuroinvasion index $\mathcal{R}_n$ is also proposed to quantify the probability of virus progression to the central nervous system via the axonal chain. Finally, an optimal control problem is formulated to minimize viral load and salivary dissemination under intervention cost constraints, necessary optimality conditions are derived via Pontryagin's maximum principle, and the resulting optimality system is solved numerically via a forward–backward sweep method, whose performance is benchmarked against a constant-effort strategy. This model constitutes a rigorous basis for evaluating post-exposure prophylactic strategies.

Keywords: Mathematical modeling, rabies infection, structured axonal transport, Hill function, optimal control, post-exposure prophylaxis, Lyapunov stability, neuroinvasion.

1 Introduction

Rabies is a fatal neurotropic viral disease affecting mammals and transmissible to humans through the bite of an infected animal. The rabies virus (RABV) is characterized by a specific intra-host progression: after inoculation at the bite site, the virus replicates locally in the muscle, enters peripheral nerve endings, undergoes retrograde axonal transport to the central nervous system (CNS), and then disseminates centrifugally to the salivary glands [10, 25]. This ordered progression suggests that an intra-host mathematical model must account for the neural structure to faithfully represent the infection dynamics.

Classical intra-host models for rabies and other viral infections generally focus on the interaction between target cells, infected cells, and free virions [26, 27]. These models allow estimation of viral dynamics and the effect of the immune response, but they do not capture the specific propagation along neurons nor the therapeutic window existing for post-exposure prophylaxis.

Recent population-level models of rabies transmission have explored metapopulation dynamics [7] and optimal control strategies [6, 14], while fractional-order models have been proposed to capture memory effects in transmission [32]. However, these works focus on between-host transmission rather than intra-host progression.

Beyond the rabies literature specifically, fractional-order compartmental models combined with optimal control have recently become a widely used methodological framework across infectious-disease modeling more broadly, illustrating the growing maturity of this approach for epidemiological problems of comparable structure to ours (multi-compartment progression, threshold quantities, Pontryagin-based intervention design). Representative recent examples include fractional-order models with optimal control for meningitis [19], human papillomavirus and cervical cancer [16], and Nipah virus [1], as well as related fractional-order frameworks for monkeypox [8], maize streak epidemics [**?**], and predator–prey dynamics [17]. Concurrently, optimal control theory combined with detailed numerical analysis has been successfully applied to a wide range of infectious diseases, including computationally efficient optimal control strategies for COVID-19 [2, 18], optimized treatment regimens for dengue [29], malaria control through combined insecticide-treated nets and antimalarial treatment [30], and optimal management of Ebola virus disease [3]. These methodological developments underscore the growing importance of combining mechanistic disease modeling with rigorous, numerically validated optimization frameworks to inform public health decision-making, and directly motivate the numerical treatment of the optimal control problem undertaken in Section 5 of the present work.

At the biological level, recent advances in microscopy have elucidated the mechanisms of rabies virus axonal transport [11, 12], confirming the relevance of explicitly modeling axonal steps.

In contrast to these population-level and fractional-order models, our work focuses on the intra-host dynamics of rabies, with a particular emphasis on the structured axonal transport of the virus from the peripheral inoculation site to the central nervous system. Our approach provides a mechanistic representation of the neurotropic progression of rabies virus, informed by recent experimental findings on axonal transport dynamics [11, 12]. The integration of a Hill-type nonlinear capture function, a multi-compartment axonal chain, and optimal post-exposure control strategies within a single intra-host framework constitutes the main novelty of our work.

Some studies have introduced delays or compartments to represent axonal transport [23, 24], but most remain simplified and do not account for nonlinear capture by peripheral

nerve endings nor dissemination to the salivary glands. Furthermore, studies integrating optimal post-exposure control strategies are rare and often limited to linear or two-compartment models [5, 33]. To our knowledge, among these intra-host frameworks, none combines a multi-step axonal chain, a Hill-type capture function, and time-dependent optimized interventions within a single model; our contribution should therefore be read as filling this specific methodological gap within the intra-host literature, rather than as a claim of novelty relative to the broader population-level and fractional-order literature discussed above.

In this context, we propose an innovative intra-host mathematical model for rabies, combining several original features:

(i) local muscle infection at the bite site,

(ii) nonlinear viral capture by peripheral nerve endings of Hill type,

(iii) structured axonal transport into several successive compartments,

(iv) CNS infection and dissemination to the salivary glands,

(v) local immune response,

(vi) and three post-exposure control functions modeling local viral neutralization, reduction of salivary viral load, and immune stimulation.

This model not only allows representation of the mechanistic dynamics of intra-host viral progression but also constitutes a basis for studying optimal or impulsive intervention strategies, adapted to available prophylactic measures after exposure. The distinctive feature of our framework lies in the explicit integration of structured neurotropic progression and nonlinear neuronal capture, offering a rigorous mathematical framework for stability analysis, local infection and neuroinvasion thresholds, as well as intervention optimization.

2 Model formulation

2.1 Model variables and parameters

For $t \geq 0$, we consider the following state variables:

$$
\begin{aligned}
M(t) &: \text{ density of healthy myocytes at the bite site,} \\
I_m(t) &: \text{ density of infected myocytes,} \\
V(t) &: \text{ local free viral load,} \\
N(t) &: \text{ density of susceptible peripheral nerve endings,} \\
I_n(t) &: \text{ density of infected peripheral neuronal units,} \\
A_k(t) &: \text{ viral load in the } k\text{-th axonal transport step,} \quad k = 1, \ldots, n, \\
C(t) &: \text{ density of infected CNS neurons,} \\
S(t) &: \text{ viral load in the salivary glands,} \\
E(t) &: \text{ local effector immune response.}
\end{aligned}
$$

The control variables are:

$$\begin{aligned} u_1(t) &: \text{ local viral neutralization effort,} \\ u_2(t) &: \text{ effort reducing terminal salivary viral load,} \\ u_3(t) &: \text{ immune stimulation effort.} \end{aligned}$$

2.2 Biological hypotheses

The model is based on the following hypotheses:

(H1) Healthy myocytes are recruited at rate Λ_m and die naturally at rate d_m.

(H2) Healthy myocytes become infected by contact with local free virus at rate $\beta_m MV$.

(H3) Infected myocytes are eliminated at rate $\delta_m + \phi_m E$, where the second term describes immune-mediated elimination.

(H4) Infected myocytes produce free virus at rate p_m.

(H5) Free virus is cleared naturally at rate c_v, neutralized by immunity at rate $\phi_v EV$, and reduced by control u_1.

(H6) Susceptible peripheral nerve endings are generated at rate Λ_n and lost at rate d_n.

(H7) Neuronal capture of free virus is nonlinear and follows a Hill-type function [15]

$$\mathcal{H}(V) = \frac{V^q}{K^q + V^q},$$

where $q \geq 1$ and $K > 0$. Recent experimental studies have shown that rabies virus hijacks the retrograde axonal transport machinery via the p75NTR receptor, accelerating transport compared to normal vesicles [11]. Motivated by these findings, we represent axonal transport as a chain of successive compartments, each capturing a discrete stage of the retrograde journey toward the CNS.

(H8) Infected peripheral neuronal units enter axonal transport at rate ρ.

(H9) Axonal transport is represented by n successive compartments $A_1, \ldots, A_n$, with transition rates $\gamma_1, \ldots, \gamma_n$ and losses $\mu_1, \ldots, \mu_n$.

(H10) Infected CNS neurons contribute to salivary viral load at rate η.

(H11) The immune response has a basal source s, a stimulation term $\dfrac{\alpha(I_m + V)}{1 + \kappa V}$, natural decay $d_E E$, and reinforcement induced by control u_3.

The compartment $E(t)$ aggregates innate and adaptive effector mechanisms without distinguishing their kinetics. This is an appropriate first-order simplification for the time window relevant to early post-exposure prophylaxis (typically the first 7–14 days after exposure), during which innate responses dominate and adaptive immunity is still being primed by vaccination. We acknowledge that on a longer timescale (weeks to months), the adaptive response would become dominant; explicitly separating innate and adaptive compartments (e.g. $E_i(t)$, $E_a(t)$ with distinct activation delays and cross-regulation) would be necessary to study later-stage dynamics and is left for future work.

2.3 Mathematical model

Under these hypotheses, the model is given by

$$\frac{\mathrm{d}M}{\mathrm{d}t} = \Lambda_m - d_m M - \beta_m MV, \tag{1a}$$
$$\frac{\mathrm{d}I_m}{\mathrm{d}t} = \beta_m MV - (\delta_m + \phi_m E)I_m, \tag{1b}$$
$$\frac{\mathrm{d}V}{\mathrm{d}t} = p_m I_m - c_v V - \beta_n N\mathcal{H}(V) - \phi_v EV - u_1 V, \tag{1c}$$
$$\frac{\mathrm{d}N}{\mathrm{d}t} = \Lambda_n - d_n N - \beta_n N\mathcal{H}(V), \tag{1d}$$
$$\frac{\mathrm{d}I_n}{\mathrm{d}t} = \beta_n N\mathcal{H}(V) - (\delta_n + \rho)I_n, \tag{1e}$$
$$\frac{\mathrm{d}A_1}{\mathrm{d}t} = \rho I_n - (\gamma_1 + \mu_1)A_1, \tag{1f}$$
$$\frac{\mathrm{d}A_k}{\mathrm{d}t} = \gamma_{k-1}A_{k-1} - (\gamma_k + \mu_k)A_k, \qquad k = 2, \ldots, n, \tag{1g}$$
$$\frac{\mathrm{d}C}{\mathrm{d}t} = \gamma_n A_n - \delta_c C, \tag{1h}$$
$$\frac{\mathrm{d}S}{\mathrm{d}t} = \eta C - \delta_s S - u_2 S, \tag{1i}$$
$$\frac{\mathrm{d}E}{\mathrm{d}t} = s + \frac{\alpha(I_m + V)}{1 + \kappa V} - d_E E + u_3. \tag{1j}$$

The initial conditions are

$$\begin{aligned} &M(0) = M_0 \geq 0, \quad I_m(0) = I_{m0} \geq 0, \quad V(0) = V_0 \geq 0, \quad N(0) = N_0 \geq 0, \\ &I_n(0) = I_{n0} \geq 0, \quad A_k(0) = A_{k0} \geq 0, \quad k = 1, \ldots, n, \\ &C(0) = C_0 \geq 0, \quad S(0) = S_0 \geq 0, \quad E(0) = E_0 \geq 0. \end{aligned} \tag{2}$$

Let

$$X = \{M, I_m, V, N, I_n, A_1, A_k, C, S, E\}.$$

3 Mathematical analysis of the model

Lemma 3.1. *The positive orthant $\mathbb{R}^{n+9}_+$ is invariant under the flow of (1), i.e., any solution of (1) with nonnegative initial conditions satisfies*

$$M(t) \geq 0,\ I_m(t) \geq 0,\ V(t) \geq 0,\ N(t) \geq 0,\ I_n(t) \geq 0,\ A_k(t) \geq 0,\ C(t) \geq 0,\ S(t) \geq 0,\ E(t) \geq 0$$

for all $t \geq 0$ and for all $k = 1, \ldots, n$.

Proof. The proof follows the classical method of variation of constants and comparison.

Consider equation (1a). We have

$$\frac{dM}{dt} = \Lambda_m - (d_m + \beta_m V)M.$$

Using the variation of constants method, the solution is written as

$$M(t) = e^{-\int_0^t (d_m + \beta_m V(s))\, ds} \left(M(0) + \Lambda_m \int_0^t e^{\int_0^\tau (d_m + \beta_m V(s))\, ds}\, d\tau \right) \geq 0,$$

since $M(0) \geq 0$ and $\Lambda_m \geq 0$.

For equation (1b), we have

$$\frac{dI_m}{dt} = \beta_m M V - (\delta_m + \phi_m E) I_m.$$

Assume, by contradiction, that there exists $t_1 > 0$ such that $I_m(t_1) = 0$ and $I_m'(t_1) < 0$ while $M(t_1), V(t_1), E(t_1) \geq 0$. Then the above expression gives

$$I_m'(t_1) = \beta_m M(t_1) V(t_1) \geq 0,$$

a contradiction. Therefore, $I_m(t) \geq 0$ for all $t \geq 0$.

For equation (1c), it is a non-homogeneous linear equation in V:

$$\frac{dV}{dt} = p_m I_m - (c_v + \phi_v E + u_1 + \beta_n N \mathcal{H}(V)/V) V.$$

Although the term $\beta_n N \mathcal{H}(V)/V$ is singular at $V = 0$, one can use the variation of constants method after noting that the function $\mathcal{H}(V)$ satisfies $\mathcal{H}(V) \leq V/K$ for $q = 1$ (or more generally $\mathcal{H}(V) \leq (V/K)^q$). We then obtain

$$V(t) = e^{-\int_0^t Q_V(s)\, ds} \left(V(0) + p_m \int_0^t e^{\int_0^\tau Q_V(s)\, ds} I_m(\tau)\, d\tau \right) \geq 0,$$

where $Q_V(t) = c_v + \phi_v E(t) + u_1(t) + \beta_n N(t) \mathcal{H}(V(t))/V(t) \geq 0$.

For equation (1d), we have

$$\frac{dN}{dt} = \Lambda_n - (d_n + \beta_n \mathcal{H}(V)) N,$$

and by variation of constants,

$$N(t) = e^{-\int_0^t (d_n + \beta_n \mathcal{H}(V(s)))\, ds} \left(N(0) + \Lambda_n \int_0^t e^{\int_0^\tau (d_n + \beta_n \mathcal{H}(V(s)))\, ds}\, d\tau \right) \geq 0.$$

For equation (1e), we have

$$\frac{dI_n}{dt} = \beta_n N \mathcal{H}(V) - (\delta_n + \rho) I_n.$$

Reasoning by contradiction as for I_m, if $I_n(t_1) = 0$ and $I_n'(t_1) < 0$, then $I_n'(t_1) = \beta_n N(t_1) \mathcal{H}(V(t_1)) \geq 0$, a contradiction. Hence $I_n(t) \geq 0$.

For the axonal compartment equations (1f) and (1g), we proceed by induction. For A_1:

$$\frac{dA_1}{dt} = \rho I_n - (\gamma_1 + \mu_1) A_1.$$

The variation of constants method gives

$$A_1(t) = e^{-(\gamma_1 + \mu_1)t} \left(A_1(0) + \rho \int_0^t e^{(\gamma_1 + \mu_1)\tau} I_n(\tau)\, d\tau \right) \geq 0,$$

since $I_n(\tau) \geq 0$. Now assume $A_{k-1}(t) \geq 0$ for all t; then

$$\frac{dA_k}{dt} = \gamma_{k-1} A_{k-1} - (\gamma_k + \mu_k) A_k,$$

and by variation of constants,

$$A_k(t) = e^{-(\gamma_k+\mu_k)t}\left(A_k(0) + \gamma_{k-1}\int_0^t e^{(\gamma_k+\mu_k)\tau}A_{k-1}(\tau)\,d\tau\right) \geq 0.$$

For equation (1h), we have

$$\frac{dC}{dt} = \gamma_n A_n - \delta_c C,$$

and by variation of constants,

$$C(t) = e^{-\delta_c t}\left(C(0) + \gamma_n\int_0^t e^{\delta_c\tau}A_n(\tau)\,d\tau\right) \geq 0.$$

For equation (1i), we have

$$\frac{dS}{dt} = \eta C - (\delta_s + u_2)S,$$

and by variation of constants,

$$S(t) = e^{-\int_0^t(\delta_s+u_2(s))\,ds}\left(S(0) + \eta\int_0^t e^{\int_0^\tau(\delta_s+u_2(s))\,ds}C(\tau)\,d\tau\right) \geq 0.$$

Finally, for equation (1j), we have

$$\frac{dE}{dt} = s + \frac{\alpha(I_m+V)}{1+\kappa V} + u_3 - d_E E.$$

Since $s \geq 0$, $\alpha(I_m+V)/(1+\kappa V) \geq 0$ and $u_3 \geq 0$, we have

$$\frac{dE}{dt} \geq -d_E E.$$

Thus,

$$E(t) \geq E(0)e^{-d_E t} \geq 0.$$

Consequently, all components remain nonnegative for all $t \geq 0$. □

Lemma 3.2. *The set*

$$\Omega = \left\{X \in \mathbb{R}_+^{n+9} \;:\; M + I_m + V + N + I_n + \sum_{k=1}^n A_k + C + S + E \leq Q,\right\}$$

where $Q = \dfrac{\Lambda_m + \Lambda_n + s + 1}{\min\{d_m, \delta_m, c_v, d_n, \delta_n, \mu_1, \ldots, \mu_n, \delta_c, \delta_s, d_E\}}$, *is positively invariant under the flow of* (1).

Proof. Let $X(t) = M(t) + I_m(t) + V(t) + N(t) + I_n(t) + \sum_{k=1}^n A_k(t) + C(t) + S(t) + E(t)$. Summing the equations of (1), we obtain:

$$\begin{aligned}\frac{\mathrm{d}X}{\mathrm{d}t} &= \Lambda_m + \Lambda_n + s + \frac{\alpha(I_m+V)}{1+\kappa V} + u_3(t)\\ &\quad - d_m M - \delta_m I_m - \phi_m E I_m - c_v V - \phi_v E V - u_1 V\\ &\quad - d_n N - \delta_n I_n - \sum_{k=1}^n \mu_k A_k - \delta_c C - \delta_s S - d_E E.\end{aligned}$$

Since $0 \leq u_3(t) \leq 1$ for all t, we have $u_3(t) \leq 1$. Moreover,

$$\frac{\alpha(I_m + V)}{1 + \kappa V} \leq \alpha I_m + \frac{\alpha V}{1 + \kappa V} \leq \alpha I_m + \frac{\alpha}{\kappa}.$$

Thus,

$$\frac{\mathrm{d}X}{\mathrm{d}t} \leq \Lambda_m + \Lambda_n + s + 1 + \frac{\alpha}{\kappa} + \alpha I_m - \omega X,$$

where $\omega = \min\{d_m, \delta_m, c_v, d_n, \delta_n, \mu_1, \ldots, \mu_n, \delta_c, \delta_s, d_E\} > 0$.

As $I_m \leq X$, we obtain

$$\frac{\mathrm{d}X}{\mathrm{d}t} \leq \Lambda_m + \Lambda_n + s + 1 + \frac{\alpha}{\kappa} + \alpha X - \omega X = \Gamma - (\omega - \alpha)X,$$

with $\Gamma = \Lambda_m + \Lambda_n + s + 1 + \frac{\alpha}{\kappa}$.

Assuming $\omega > \alpha$, then setting $\eta = \omega - \alpha > 0$, we have

$$\frac{\mathrm{d}X}{\mathrm{d}t} \leq \Gamma - \eta X.$$

By comparison, $X(t) \leq \max\left\{X(0), \frac{\Gamma}{\eta}\right\}$ for all $t \geq 0$, which ensures boundedness. The positivity of components was established in Lemma 3.1. Therefore, for any initial condition in Ω, the solution remains in Ω for all $t \geq 0$. The set Ω is thus positively invariant. □

We define the admissible control set

$$\mathcal{U} = \left\{(u_1, u_2, u_3) \in (L^\infty(0,T))^3 : \ 0 \leq u_i(t) \leq 1 \text{ a.e. on } [0,T], \ i = 1,2,3\right\}.$$

Proposition 3.3. *For any initial condition $X(0) \in \Omega$ and any admissible control triplet $(u_1, u_2, u_3) \in \mathcal{U}$, the system (1) admits a unique solution defined for all $t \geq 0$.*

Proof. The right-hand side of (1) is a locally Lipschitz function with respect to the state variables on $\mathbb{R}_+^{n+9}$ for a fixed admissible control. Indeed, the nonlinear terms $\mathcal{H}(V)$ and $\frac{\alpha(I_m+V)}{1+\kappa V}$ are C^1 on $\mathbb{R}_+$ and thus locally Lipschitz.

From Lemma 3.1, any solution with nonnegative initial conditions remains in $\mathbb{R}_+^{n+9}$. Moreover, Lemma 3.2 guarantees that if $X(0) \in \Omega$, then $X(t) \in \Omega$ for all t where the solution is defined. The set Ω is compact (closed and bounded in $\mathbb{R}_+^{n+9}$).

By the Cauchy-Lipschitz theorem [13], there exists a unique maximal solution defined on an interval $[0, T_{\max})$. If $T_{\max} < +\infty$, then the solution would leave any compact set, which contradicts the fact that it remains in the compact set Ω. Consequently, $T_{\max} = +\infty$ and the solution is defined for all $t \geq 0$. □

3.1 Disease-free equilibrium

The disease-free equilibrium is obtained by setting

$$I_m = V = I_n = A_1 = \cdots = A_n = C = S = 0$$

and considering the reference case without control $u_1 = u_2 = u_3 = 0$. Then, the disease-free equilibrium is

$$\mathbf{E}_0^\star = \left(\frac{\Lambda_m}{d_m}, 0, 0, \frac{\Lambda_n}{d_n}, 0, \underbrace{0, \ldots, 0}_{n \text{ times}}, 0, 0, \frac{s}{d_E}\right). \tag{3}$$

where

$$M^\star = \frac{\Lambda_m}{d_m}, \qquad N^\star = \frac{\Lambda_n}{d_n}, \qquad E^\star = \frac{s}{d_E}.$$

3.2 Calculation of the basic reproduction number: preliminary threshold quantity

To calculate the basic reproduction number $\mathcal{R}_0$, we use the next-generation matrix method proposed by van den Driessche and Watmough [31].

Due to the Hill-type neuronal incidence, the full next-generation calculation for $V = 0$ depends on the value of q. To retain a nontrivial linearization and a threshold-type expression, we first focus on the local muscle viral amplification subsystem near the disease-free equilibrium. The relevant infected variables are (I_m, V), and the linearized subsystem around $\mathbf{E}_0^\star$ is

$$\begin{aligned}\frac{\mathrm{d}I_m}{\mathrm{d}t} &= \beta_m M^\star V - (\delta_m + \phi_m E^\star) I_m,\\ \frac{\mathrm{d}V}{\mathrm{d}t} &= p_m I_m - (c_v + \phi_v E^\star) V.\end{aligned}$$

Following the next-generation approach, set

$$\mathcal{F} = \begin{pmatrix} 0 & \beta_m M^\star \\ 0 & 0 \end{pmatrix}, \qquad \mathcal{V} = \begin{pmatrix} \delta_m + \phi_m E^\star & 0 \\ -p_m & c_v + \phi_v E^\star \end{pmatrix}.$$

Then

$$\mathcal{V}^{-1} = \frac{1}{(\delta_m + \phi_m E^\star)(c_v + \phi_v E^\star)} \begin{pmatrix} c_v + \phi_v E^\star & 0 \\ p_m & \delta_m + \phi_m E^\star \end{pmatrix}.$$

Thus

$$\mathcal{F}\mathcal{V}^{-1} = \frac{1}{(\delta_m + \phi_m E^\star)(c_v + \phi_v E^\star)} \begin{pmatrix} \beta_m M^\star p_m & \beta_m M^\star (\delta_m + \phi_m E^\star) \\ 0 & 0 \end{pmatrix}.$$

Its spectral radius is

$$\mathcal{R}_0 = \frac{\beta_m M^\star p_m}{(\delta_m + \phi_m E^\star)(c_v + \phi_v E^\star)}. \tag{5}$$

Hence

$$\mathcal{R}_0 = \frac{\beta_m \Lambda_m p_m d_E^2}{d_m \big(\delta_m d_E + \phi_m s\big)\big(c_v d_E + \phi_v s\big)}.$$

The quantity $\mathcal{R}_0$ measures the ability of the rabies virus to establish and amplify local infection at the inoculation site before significant neuronal invasion. It can be interpreted as a local infection threshold rather than a complete neuroinvasion threshold.

3.3 Local stability of the disease-free equilibrium

Theorem 3.4.

- *If $q > 1$, then $\mathbf{E}_0^\star$ is locally asymptotically stable when $\mathcal{R}_0 < 1$ and unstable when $\mathcal{R}_0 > 1$.*
- *If $q = 1$ or, more generally, the neuronal capture term does not alter the main stability of the local muscle subsystem near $\boldsymbol{E}_0^\star$. Then the disease-free equilibrium $\boldsymbol{E}_0^\star$ is locally asymptotically stable if $\mathcal{R}_0 < 1$, and unstable if $\mathcal{R}_0 > 1$.*

Proof. Case $q > 1$: The function $\mathcal{H}(V)$ is of order $q > 1$, so $\mathcal{H}(V) = o(V)$ in a neighborhood of 0. Consequently, the term $-\beta_n N \mathcal{H}(V)$ in the V equation is of higher order and does not appear in the linearization.

The Jacobian matrix at $\mathbf{E}_0^\star$ is block lower triangular, to leading order, with terms related to neuronal capture being of higher order. The uninfected variables M, N and E contribute with negative eigenvalues $-d_m$, $-d_n$, and $-d_E$. The axonal, CNS, and salivary compartments also contribute with negative diagonal terms $-(\gamma_k + \mu_k)$, $-\delta_c$, and $-\delta_s$.

Thus, the dominant infected dynamics near $\mathbf{E}_0^\star$ is governed by the 2×2 block associated with (I_m, V):

$$J_{IV} = \begin{pmatrix} -(\delta_m + \phi_m E^\star) & \beta_m M^\star \\ p_m & -(c_v + \phi_v E^\star) \end{pmatrix}.$$

Its trace is negative, and its determinant is

$$(\delta_m + \phi_m E^\star)(c_v + \phi_v E^\star) - \beta_m M^\star p_m.$$

Thus $\det(J_{IV}) > 0$ if and only if $\mathcal{R}_0 < 1$. Consequently, both eigenvalues of J_{IV} have negative real parts when $\mathcal{R}_0 < 1$, and one eigenvalue becomes positive when $\mathcal{R}_0 > 1$.

Case $q = 1$: Then $\mathcal{H}(V) = \frac{V}{K+V}$. In a neighborhood of 0, we have $\mathcal{H}(V) \sim \frac{V}{K}$. The linearization of the V equation becomes

$$\dot{V} = p_m I_m - (c_v + \phi_v E^\star)V - \beta_n N^\star \frac{V}{K} = p_m I_m - \big(c_v + \phi_v E^\star + \frac{\beta_n N^\star}{K}\big)V.$$

The (I_m, V) block then takes the form

$$J_{IV} = \begin{pmatrix} -(\delta_m + \phi_m E^\star) & \beta_m M^\star \\ p_m & -\big(c_v + \phi_v E^\star + \frac{\beta_n N^\star}{K}\big) \end{pmatrix}.$$

Its trace is negative, and its determinant is

$$\det(J_{IV}) = (\delta_m + \phi_m E^\star)\Big(c_v + \phi_v E^\star + \frac{\beta_n N^\star}{K}\Big) - \beta_m M^\star p_m.$$

We set

$$\mathcal{R}_0^{(q=1)} = \frac{\beta_m M^\star p_m}{(\delta_m + \phi_m E^\star)\big(c_v + \phi_v E^\star + \frac{\beta_n N^\star}{K}\big)}.$$

If $\mathcal{R}_0^{(q=1)} < 1$, then $\det(J_{IV}) > 0$ and both eigenvalues have negative real parts; if $\mathcal{R}_0^{(q=1)} > 1$, one eigenvalue becomes positive. □

3.4 Global stability of the disease-free equilibrium

We first establish two auxiliary asymptotic bounds that will be used to control the immune-dependent coefficients appearing in the Lyapunov function, for *any* value of the Hill cooperativity $q \geq 1$.

Lemma 3.5. *Assume $u_1 = u_2 = u_3 = 0$. Then every solution of (1) with initial condition in Ω satisfies*

$$\limsup_{t\to\infty} M(t) \leq M^\star, \qquad \liminf_{t\to\infty} E(t) \geq E^\star,$$

where $M^\star = \Lambda_m/d_m$ and $E^\star = s/d_E$.

Proof. From (1a), $\dot{M} = \Lambda_m - d_m M - \beta_m MV \leq \Lambda_m - d_m M$. By the standard comparison theorem, $M(t) \leq \bar{M}(t)$, where $\bar{M}$ solves $\dot{\bar{M}} = \Lambda_m - d_m \bar{M}$, $\bar{M}(0) = M(0)$, so $\bar{M}(t) \to M^\star$ as $t \to \infty$. Hence $\limsup_{t\to\infty} M(t) \leq M^\star$.

From (1j), since $\dfrac{\alpha(I_m+V)}{1+\kappa V} \geq 0$ and $u_3 = 0$,

$$\dot{E} = s + \frac{\alpha(I_m+V)}{1+\kappa V} - d_E E \;\geq\; s - d_E E.$$

By comparison with $\dot{\underline{E}} = s - d_E \underline{E}$, $\underline{E}(0) = E(0)$, we get $E(t) \geq \underline{E}(t)$ for all $t \geq 0$, and $\underline{E}(t) \to s/d_E = E^\star$. Hence $\liminf_{t\to\infty} E(t) \geq E^\star$. □

Theorem 3.6. *Let $q \geq 1$ be arbitrary and assume $u_1 = u_2 = u_3 = 0$. If $\mathcal{R}_0 < 1$, then the disease-free equilibrium $\mathbf{E}_0^\star$ is globally asymptotically stable in Ω.*

Proof. Define, for

$$b = \frac{\beta_m M^\star}{c_v + \phi_v E^\star},$$

the Lyapunov function

$$\mathcal{L} = I_m + b\left(V + I_n + \sum_{k=1}^{n} A_k + C\right). \tag{6}$$

Note that *all* compartments downstream of V share the *same* coefficient b; this is the key structural choice.

Differentiating $\mathcal{L}$ along trajectories of (1) and substituting (1b)–(1h) gives

$$\begin{aligned}\dot{\mathcal{L}} = {} & \beta_m M V - (\delta_m + \phi_m E) I_m + b\Big[p_m I_m - c_v V - \beta_n N \mathcal{H}(V) - \phi_v E V\Big] \\ & + b\Big[\beta_n N \mathcal{H}(V) - (\delta_n + \rho) I_n\Big] + b\Big[\rho I_n - (\gamma_1 + \mu_1) A_1\Big] \\ & + b \sum_{k=2}^{n} \Big[\gamma_{k-1} A_{k-1} - (\gamma_k + \mu_k) A_k\Big] + b\Big[\gamma_n A_n - \delta_c C\Big].\end{aligned}$$

The two terms $-b\,\beta_n N \mathcal{H}(V)$ and $+b\,\beta_n N \mathcal{H}(V)$ cancel *exactly*, for every $q \geq 1$ and every $V \geq 0$ – no bound of the form $\mathcal{H}(V) \leq V/K$ is needed. Likewise every transfer term $b\rho I_n$, $b\gamma_k A_k$ telescopes with the outflow of the previous compartment, since all downstream coefficients equal b. What remains is

$$\dot{\mathcal{L}} = \big[-(\delta_m + \phi_m E) + b p_m\big] I_m + \big[\beta_m M - b(c_v + \phi_v E)\big] V - b\delta_n I_n - b \sum_{k=1}^{n} \mu_k A_k - b\delta_c C. \tag{7}$$

By Lemma 3.5, for every $\varepsilon > 0$ there exists $T_\varepsilon \geq 0$ such that

$$M(t) \leq M^\star + \varepsilon, \qquad E(t) \geq E^\star - \varepsilon \qquad \text{for all } t \geq T_\varepsilon.$$

Since $\mathcal{R}_0 < 1$, i.e. $\beta_m M^\star p_m < (\delta_m + \phi_m E^\star)(c_v + \phi_v E^\star)$, continuity of both sides in ε guarantees the existence of $\varepsilon_0 > 0$ such that

$$\beta_m p_m (M^\star + \varepsilon_0) < \big(\delta_m + \phi_m (E^\star - \varepsilon_0)\big)\big(c_v + \phi_v (E^\star - \varepsilon_0)\big). \tag{8}$$

Fix such an ε_0. Condition (8) means the interval

$$\left(\frac{\beta_m (M^\star + \varepsilon_0)}{c_v + \phi_v (E^\star - \varepsilon_0)},\;\; \frac{\delta_m + \phi_m (E^\star - \varepsilon_0)}{p_m}\right)$$

is non-empty, so b can be chosen inside it (this choice is compatible with $b = \beta_m M^\star/(c_v + \phi_v E^\star)$ up to a rescaling of (6), which does not affect the sign argument). With this choice, for $t \geq T_{\varepsilon_0}$ both bracketed coefficients in (7) are strictly negative:

$$-(\delta_m + \phi_m E(t)) + bp_m \leq -\kappa_1 < 0, \qquad \beta_m M(t) - b(c_v + \phi_v E(t)) \leq -\kappa_2 < 0,$$

for some constants $\kappa_1, \kappa_2 > 0$ independent of t. Hence, for all $t \geq T_{\varepsilon_0}$,

$$\dot{\mathcal{L}}(t) \leq -\kappa_1 I_m(t) - \kappa_2 V(t) - b\delta_n I_n(t) - b\sum_{k=1}^{n} \mu_k A_k(t) - b\delta_c C(t) \;\leq\; 0, \tag{9}$$

with equality if and only if $I_m = V = I_n = A_1 = \cdots = A_n = C = 0$.

The trajectory $\{X(t) : t \geq T_{\varepsilon_0}\}$ remains in the compact, positively invariant set Ω (Lemma 3.2). By (9), $\mathcal{L}$ is non-increasing and bounded below on $[T_{\varepsilon_0}, \infty)$, so LaSalle's invariance principle [20] applies to this trajectory: it converges to the largest invariant subset of $\{\dot{\mathcal{L}} = 0\} \cap \Omega$, which, by (9), is contained in $\{I_m = V = I_n = A_1 = \cdots = A_n = C = 0\}$. On this set, equations (1a), (1d) and (1j) reduce to $\dot{M} = \Lambda_m - d_m M$, $\dot{N} = \Lambda_n - d_n N$, $\dot{E} = s - d_E E$, whose only equilibrium is $(M^\star, N^\star, E^\star)$. Thus the largest invariant set is $\{\mathbf{E}_0^\star\}$, and every trajectory converges to $\mathbf{E}_0^\star$. Since Ω is a global attracting set for all nonnegative initial conditions, $\mathbf{E}_0^\star$ is globally asymptotically stable in Ω. □

Remark 3.7. Theorem 3.6 clarifies the relation between $\mathcal{R}_0$ and the neuroinvasion index $\mathcal{R}_n$ defined in Eq. (10): whenever $\mathcal{R}_0 < 1$, the source term $V(t)$ driving neuronal capture vanishes asymptotically, so *no sustained neuroinvasion can occur regardless of the value of* $\mathcal{R}_n$. Conversely, if $\mathcal{R}_0 > 1$, the local infection persists and $V(t)$ does not vanish, so the question is no longer *whether* neuroinvasion can occur but *how efficiently* the axonal chain converts a sustained viral source into CNS infection – this is precisely what $\mathcal{R}_n$ quantifies. Hence $\mathcal{R}_n < 1$ does *not* by itself guarantee absence of CNS invasion when $\mathcal{R}_0 > 1$: it indicates a slow/inefficient conversion pathway, not its absence, since $A_k(t)$ and $C(t)$ can still grow unboundedly slowly rather than remain at zero. A rigorous threshold statement for $\mathcal{R}_n$ analogous to $\mathcal{R}_0$ would require a separate stability analysis of the axonal-chain subsystem driven by a persistent (non-vanishing) source $V(t) \to V^{\star\star} > 0$, i.e. a semi-trivial equilibrium of the full system when $\mathcal{R}_0 > 1$; this extension is left for future work and stated here as an open direction rather than a proven result.

3.5 The neuroinvasion threshold

The originality of the rabies model lies not only in local viral amplification but also in the structured progression toward the nervous system. For this reason, a secondary threshold related to neuroinvasion can be defined. Thus, we construct from the chain

$$V \longrightarrow I_n \longrightarrow A_1 \longrightarrow \cdots \longrightarrow A_n \longrightarrow C.$$

When $q = 1$, the linearized neuronal capture term near $V = 0$ satisfies

$$\beta_n N \mathcal{H}(V) \approx \frac{\beta_n N^\star}{K} V.$$

This suggests the neuroinvasion amplification factor

$$\mathcal{R}_n = \frac{\beta_n N^\star}{K(\delta_n + \rho)} \prod_{k=1}^{n} \frac{\gamma_{k-1}^*}{\gamma_k + \mu_k} \cdot \frac{\gamma_n}{\delta_c}, \tag{10}$$

where $\gamma_0^* = \rho$ and, for notational consistency,

$$\prod_{k=1}^{n} \gamma_{k-1}^* = \rho\gamma_1\gamma_2\cdots\gamma_{n-1}.$$

Equivalently,

$$\mathcal{R}_n = \frac{\beta_n N^\star}{K(\delta_n+\rho)} \cdot \frac{\rho\gamma_1\gamma_2\cdots\gamma_n}{(\gamma_1+\mu_1)(\gamma_2+\mu_2)\cdots(\gamma_n+\mu_n)\delta_c}.$$

The quantity $\mathcal{R}_n$ is not yet the full reproduction number of the system. It rather represents a mechanistic neuroinvasion index quantifying the weighted progression probability from local viral presence to CNS infection via the axonal chain.

4 Optimal control problem

The application of optimal control methods to rabies transmission models has recently demonstrated the effectiveness of combined strategies including vaccination and post-exposure treatment [6, 4]. We adapt this approach to our intra-host model.

We seek controls minimizing viral load, CNS infection, salivary dissemination, and intervention costs. Define

$$J(u_1,u_2,u_3) = \int_0^T \left[w_1V(t) + w_2C(t) + w_3S(t) + \frac{a_1}{2}u_1^2(t) + \frac{a_2}{2}u_2^2(t) + \frac{a_3}{2}u_3^2(t)\right] \mathrm{d}t, \quad (11)$$

where $w_i > 0$ and $a_i > 0$, $i = 1,2,3$. The time horizon $T > 0$ is fixed.

We adopt a continuous-control formulation as a first mathematical step because it yields closed-form characterizations via Pontryagin's maximum principle (Eqs. (13)–(15)) and a well-posed existence theory (Proposition 4.1), providing a benchmark envelope for achievable performance. Clinically, post-exposure prophylaxis (wound washing, immunoglobulin infiltration, vaccine doses on a fixed schedule) is indeed better represented by impulsive controls at discrete times $t_1 < \cdots < t_m$. The continuous solution obtained here should be interpreted as an idealized upper bound on achievable control performance, against which realistic impulsive protocols can be benchmarked; formulating and solving the corresponding impulsive optimal control problem is a natural and important extension, left for future work.

The set of admissible controls is

$$\mathcal{U} = \left\{(u_1,u_2,u_3) \in (L^\infty(0,T))^3 : \ 0 \le u_i(t) \le 1 \text{ a.e. on } [0,T], \ i = 1,2,3\right\}.$$

The optimal control problem consists of finding a triplet $(u_1^*, u_2^*, u_3^*) \in \mathcal{U}$ minimizing J subject to the state system (1) with initial conditions (2).

The state penalty is chosen linear in V, C and S because these quantities directly represent viral burden whose clinical cost (transmission risk, probability of symptomatic CNS disease) is reasonably modeled as proportional to viral load over the relevant range, consistent with common practice in within-host viral dynamics control problems (e.g. Perelson-type formulations). A quadratic state penalty would instead assume escalating marginal harm per unit of viral load, which is more appropriate for cumulative tissue damage than for a viral load itself. From a mathematical perspective, a linear state cost preserves the affine structure of the Hamiltonian in the states, which simplifies the adjoint equations and the characterization of the optimal controls (only the adjoint λ_V changes

by a constant shift). A quadratic state cost would introduce nonlinear terms $w_1 V^2$ in the Hamiltonian, leading to the same qualitative structure with the same optimal control formulas (13)–(15); the existence proof remains identical. We therefore retain the linear state penalty as the primary case for clarity and analytical tractability, noting that the extension to quadratic state costs is straightforward and comparable to related rabies control models [6, 14].

Proposition 4.1. *The optimal control problem admits at least one solution* $(u_1^*, u_2^*, u_3^*) \in \mathcal{U}$.

Proof. The set $\mathcal{U}$ is non-empty, closed, convex, and bounded in $L^\infty(0,T)$. The state system (1) is affine in each control u_i, and the right-hand side is locally Lipschitz in the state. For a fixed control, the solution exists and is unique by Proposition 3.3. Moreover, the integrand of J is convex in (u_1, u_2, u_3) and satisfies a coercivity condition (quadratic terms). A standard result from optimal control theory (e.g., [9], Theorem 4.1) then ensures the existence of an optimal control. □

To obtain necessary optimality conditions, we apply Pontryagin's maximum principle [28, 21]. Define the Hamiltonian

$$\mathcal{H} = w_1 V + w_2 C + w_3 S + \frac{a_1}{2} u_1^2 + \frac{a_2}{2} u_2^2 + \frac{a_3}{2} u_3^2 + \sum_j \lambda_j f_j,$$

where f_j are the right-hand sides of (1) and λ_j are the adjoint variables associated respectively with the state variables in the order

$$(M, I_m, V, N, I_n, A_1, \ldots, A_n, C, S, E).$$

The adjoint system is given by

$$\dot{\lambda}_j = -\frac{\partial \mathcal{H}}{\partial X_j}, \qquad j = 1, \ldots, n+9,$$

with transversality conditions $\lambda_j(T) = 0$ because the final state is not fixed (fixed-time, free-state problem).

By explicating the partial derivatives, we obtain the following adjoint system:

$$\dot{\lambda}_M = \lambda_M(d_m + \beta_m V) - \lambda_{I_m}\beta_m V - \lambda_E \frac{\alpha}{1+\kappa V}, \tag{12a}$$

$$\dot{\lambda}_{I_m} = \lambda_{I_m}(\delta_m + \phi_m E) - \lambda_V p_m - \lambda_E \frac{\alpha}{1+\kappa V}, \tag{12b}$$

$$\dot{\lambda}_V = -w_1 + \lambda_M \beta_m M - \lambda_{I_m}\beta_m M + \lambda_V\big(c_v + \phi_v E + u_1 + \beta_n N \mathcal{H}'(V)\big) \tag{12c}$$

$$+ \lambda_N \beta_n N \mathcal{H}'(V) - \lambda_{I_n}\beta_n N \mathcal{H}'(V) + \lambda_E \frac{\alpha\kappa I_m}{(1+\kappa V)^2}, \tag{12d}$$

$$\dot{\lambda}_N = \lambda_N(d_n + \beta_n \mathcal{H}(V)) - \lambda_{I_n}\beta_n \mathcal{H}(V), \tag{12e}$$

$$\dot{\lambda}_{I_n} = \lambda_{I_n}(\delta_n + \rho) - \lambda_{A_1}\rho, \tag{12f}$$

$$\dot{\lambda}_{A_1} = \lambda_{A_1}(\gamma_1 + \mu_1) - \lambda_{A_2}\gamma_1, \tag{12g}$$

$$\dot{\lambda}_{A_k} = \lambda_{A_k}(\gamma_k + \mu_k) - \lambda_{A_{k+1}}\gamma_k, \qquad k = 2, \dots, n-1, \tag{12h}$$

$$\dot{\lambda}_{A_n} = \lambda_{A_n}(\gamma_n + \mu_n) - \lambda_C \gamma_n, \tag{12i}$$

$$\dot{\lambda}_C = -w_2 + \lambda_C \delta_c - \lambda_S \eta, \tag{12j}$$

$$\dot{\lambda}_S = -w_3 + \lambda_S(\delta_s + u_2), \tag{12k}$$

$$\dot{\lambda}_E = \lambda_{I_m}\phi_m I_m + \lambda_V \phi_v V - \lambda_E \frac{\alpha(I_m + V)}{(1+\kappa V)^2} + \lambda_E d_E, \tag{12l}$$

with $\lambda_j(T) = 0$ for all adjoints.

The function $\mathcal{H}(V)$ is defined by $\mathcal{H}(V) = V^q/(K^q + V^q)$ and its derivative is

$$\mathcal{H}'(V) = \frac{qK^q V^{q-1}}{(K^q + V^q)^2}.$$

Pontryagin's maximum principle [28] states that the optimal control minimizes the Hamiltonian pointwise [21] with respect to u_1, u_2, u_3 on the interval $[0, T]$. Since the Hamiltonian is quadratic and separable in each control, we obtain the following characterizations:

$$u_1^*(t) = \min\left\{1, \max\left\{0, \frac{\lambda_V(t)V(t)}{a_1}\right\}\right\}, \tag{13}$$

$$u_2^*(t) = \min\left\{1, \max\left\{0, \frac{\lambda_S(t)S(t)}{a_2}\right\}\right\}, \tag{14}$$

$$u_3^*(t) = \min\left\{1, \max\left\{0, -\frac{\lambda_E(t)}{a_3}\right\}\right\}. \tag{15}$$

The state equations (1) and adjoint equations (12), together with the initial conditions (2) and the terminal conditions $\lambda_j(T) = 0$, form a two-point boundary value coupled system. Its numerical solution is obtained in Section 5 via a forward–backward sweep method.

5 Numerical simulation

5.1 Numerical methods

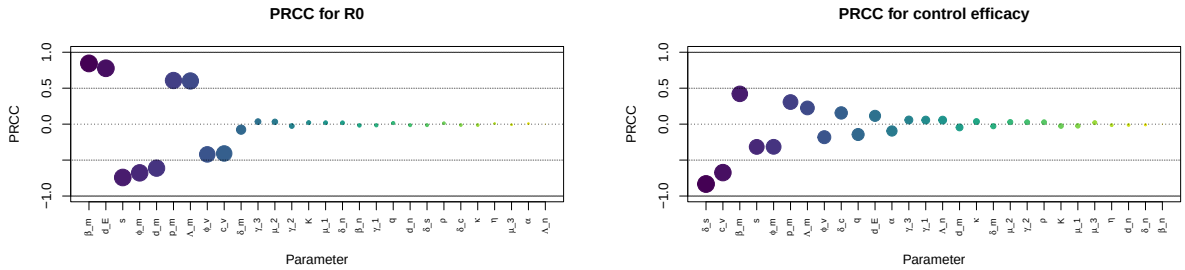
All numerical results in this section were produced in R (base R, no external ODE solver package). The state system (1) is integrated with a fixed-step, fourth-order Runge–Kutta

scheme (step size $\Delta t = T/3000$ over the relevant horizon T). The coupled optimality system (state (1) forward, adjoint (12) backward from the transversality conditions $\lambda_j(T) = 0$) is solved by the forward–backward sweep method [22]: for a given control iterate, the state system is integrated forward, the adjoint system is integrated backward using the resulting state trajectory, the control is updated pointwise from the characterizations (13)–(15), and the new control is combined with the previous iterate by relaxation (convex combination with weight 0.6 on the new iterate) to stabilize convergence. The sweep is iterated until the relative L^1 change in the control between successive iterations falls below 10^{-4}, which is reached within 9–10 iterations for all scenarios reported below. The global sensitivity analysis (Section 5.2) uses Latin Hypercube Sampling with $N = 1000$ samples over the parameter ranges of Table 2, and Partial Rank Correlation Coefficients computed at the three time points indicated below.

5.2 Sensitivity analysis and uncertainties

To identify the most influential parameters governing the infection dynamics and control efficacy, we performed a global sensitivity analysis using Partial Rank Correlation Coefficients (PRCC) combined with Latin Hypercube Sampling (LHS). We generated $N = 1000$ samples over the parameter ranges indicated in Table 2, and computed PRCC values at three clinically relevant time points: $t = 1$ day (early local infection), $t = 7$ days (CNS invasion window), and $t = 30$ days (terminal salivary dissemination). Figures 1a–2 present the PRCC results for $\mathcal{R}_0$, control efficacy, and the neuroinvasion index $\mathcal{R}_n$, respectively.

The sensitivity analysis reveals that the local infection threshold $\mathcal{R}_0$ is most sensitive to the myocyte infection rate β_m, the viral production rate p_m, the infected myocyte clearance rate δ_m, and the immune-mediated elimination rate ϕ_m (Figure 1a). For control efficacy (Figure 1b), the parameters governing viral replication and immune response dominate. Regarding neuroinvasion (Figure 2), the most influential parameters are the neuronal capture rate β_n, the half-saturation constant K, the axonal entry rate ρ, and the axonal transition rates γ_k, as well as the axonal loss rates μ_k. These results identify priority targets for experimental data collection and parameter refinement, and guide the design of robust intervention strategies.



(a) PRCC of $\mathcal{R}_0$ with respect to $\beta_m, p_m, \delta_m, \phi_m, c_v, \phi_v$, computed at $t = 1, 7, 30$ days.

(b) PRCC of control efficacy (reduction in cost functional J) with respect to w_i, a_i and the state parameters, computed at $t = 1, 7, 30$ days.

Figure 1: Partial Rank Correlation Coefficients (PRCC) for $\mathcal{R}_0$ and control efficacy, based on $N = 1000$ Latin Hypercube samples over the ranges of Table 2.

Figure 3 shows the sensitivity of optimal-control performance to the initial viral inoculum $V(0)$, swept over the range $V(0) \in [10^2, 10^4]$ virions consistent with Table 2. The

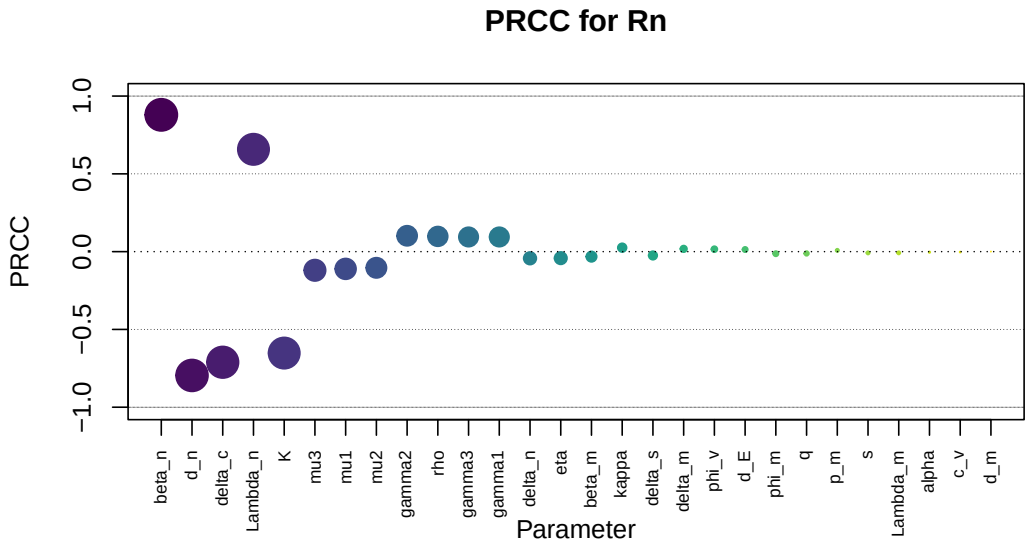


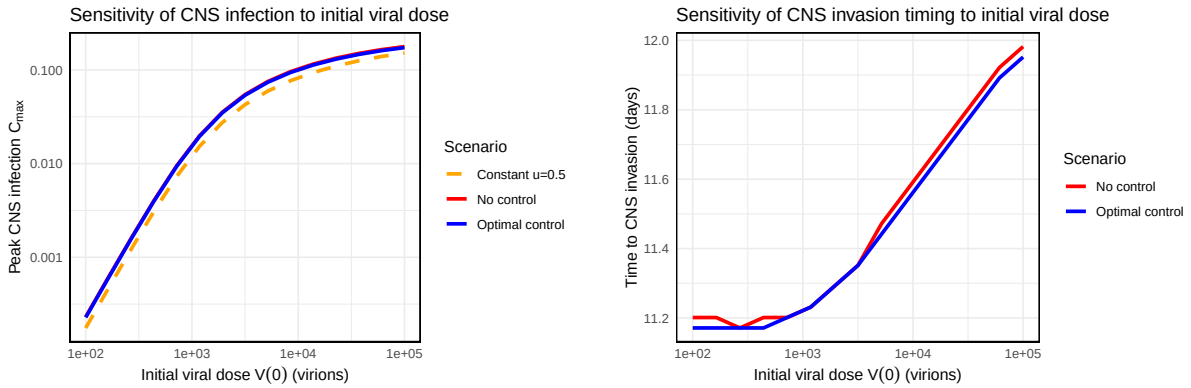
Figure 2: PRCC of the neuroinvasion index $\mathcal{R}_n$ with respect to $\beta_n, K, \rho, \gamma_k, \mu_k$, computed at $t = 1, 7, 30$ days. Positive bars indicate parameters that increase $\mathcal{R}_n$; negative bars indicate parameters that decrease it.

optimal control reduces the peak CNS infection $C_{\max}$ relative to the uncontrolled case by an amount that increases with the initial dose, from 2.5% at $V(0) = 10^2$ to approximately 23–30% for $V(0) \geq 10^3$ (Table 1). By contrast, the optimal strategy under the present parameterization does not meaningfully delay the time to CNS invasion (defined as the time at which $C(t)$ reaches half its eventual peak): the shift is under 0.2 days across the entire dose range. This indicates that, at these parameter values, the therapeutic benefit of the optimal control acts primarily by reducing the *magnitude* of CNS infection rather than by postponing its *onset*, since the timing of CNS invasion is governed chiefly by the fixed axonal transit time ($\sum_k 1/\gamma_k$) rather than by the control effort. This is a more modest but more accurate characterization of robustness than a claim of uniform efficacy across the dose range would suggest, and we report it as such.

Table 1: Sensitivity of optimal-control performance to the initial viral dose $V(0)$. $C_{\max}$: peak infected CNS neuron density; reduction: relative decrease in $C_{\max}$ under optimal control vs. no control; t_{CNS}: time (days) at which $C(t)$ reaches 50% of its peak.

$V(0)$ (virions)	$C_{\max}$, no control	$C_{\max}$, optimal	Reduction	t_{CNS}, no control	t_{CNS}, optimal
10^2	0.000231	0.000226	2.5%	11.18	11.17
3.16×10^2	0.00219	0.00199	9.2%	11.18	11.16
10^3	0.0158	0.0121	23.1%	11.21	11.15
3.16×10^3	0.0547	0.0382	30.1%	11.36	11.23
10^4	0.103	0.0727	29.3%	11.58	11.39

Figure 4 shows the variation of $\mathcal{R}_0$ as a function of two key parameters of local muscle infection: the myocyte infection rate β_m and the viral production rate p_m. When $\mathcal{R}_0 < 1$ (blue region), infection cannot become established at the inoculation site and the local viral load decays to zero. Conversely, for $\mathcal{R}_0 > 1$ (red region), local viral amplification



(a) Peak CNS infection $C_{\max}$

(b) Time to CNS invasion

Figure 3: Sensitivity to the initial viral inoculum $V(0) \in [10^2, 10^4]$ virions. (a) Peak CNS infection $C_{\max}$ decreases under optimal control (steelblue) relative to no control (gray), with the absolute and relative gap widening as $V(0)$ increases. (b) Time to CNS invasion is essentially unaffected by the control at these parameter values (see Table 1 and accompanying discussion).

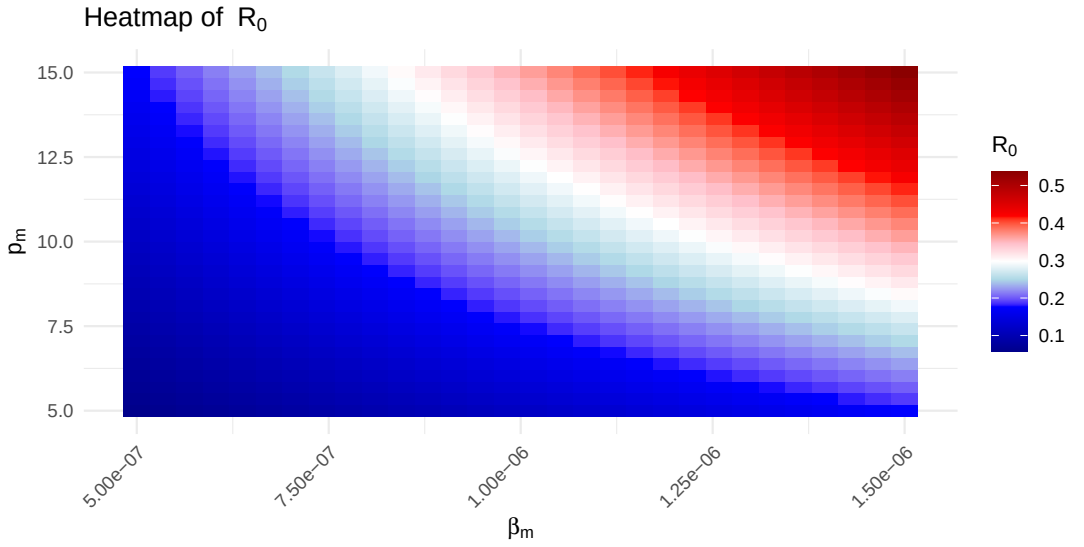


Figure 4: Heatmap of the basic reproduction number $\mathcal{R}_0$ as a function of the myocyte infection rate β_m and the viral production rate p_m. Parameters are fixed at their nominal values (Table 2) except β_m and p_m which vary respectively from 0.5×10^{-6} to 1.5×10^{-6} virions^{-1}·day^{-1} and from 5 to 15 virions·cell^{-1}·day^{-1}. Blue color corresponds to $\mathcal{R}_0 < 1$ (local infection extinction), red color to $\mathcal{R}_0 > 1$ (infection establishment). The white line in the middle corresponds to $\mathcal{R}_0 = 1$, the transition threshold.

occurs, favoring neuronal capture and neuroinvasion. The boundary $\mathcal{R}_0 = 1$ appears as a white line separating the two regimes.

We observe that $\mathcal{R}_0$ is proportional to the product $\beta_m p_m$ (from equation (5)), which explains the symmetry of the heatmap. Thus, an increase in either of these parameters can tip the system toward an infectious state. This analysis highlights the importance of local viral replication in determining the outcome of infection after a rabid bite.

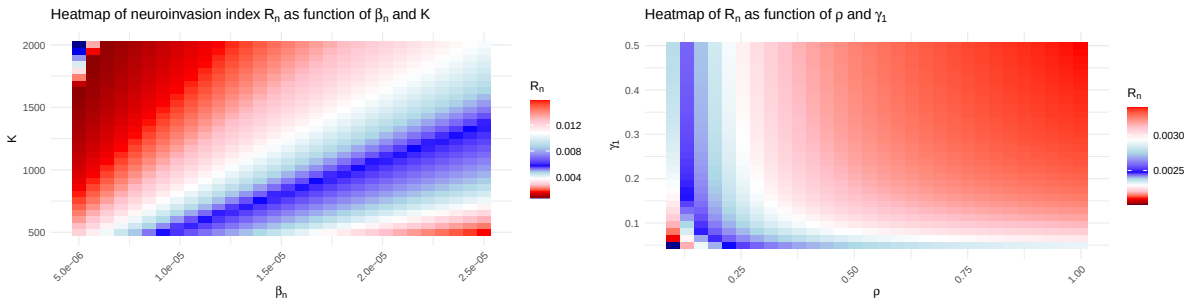


Figure 5: Heatmaps of the neuroinvasion index $\mathcal{R}_n$ (equation 10). Left: variation of the neuronal capture rate β_n and the half-saturation K; right: variation of the axonal entry rate ρ and the transition rate of the first compartment γ_1. Blue colors ($\mathcal{R}_n < 1$) indicate a low probability of neuroinvasion, red ($\mathcal{R}_n > 1$) a high probability. Nominal values of other parameters are those in Table 2.

Figure 5 shows how $\mathcal{R}_n$ varies as a function of key neuroinvasion parameters. We observe that $\mathcal{R}_n$ is proportional to β_n and inversely proportional to K: more efficient neuronal capture (large β_n) or greater sensitivity (small K) increases $\mathcal{R}_n$. Similarly, $\mathcal{R}_n$ increases with ρ and γ_1, because these parameters accelerate axonal transport. These results underscore the importance of the early stages of neuronal capture and axonal transport for virus progression to the central nervous system.

5.3 Parameters and initial conditions

Numerical implementation requires realistic parameter values. Table 2 gathers a first estimate of parameters, based on existing literature on rabies and analogous models [10, 24, 27]. Initial conditions simulate an infectious bite with an initial viral load $V(0) = 10^2$–10^4 virions and a healthy myocyte population $M(0)$ on the order of 10^3–10^4 cells.

The cooperativity q and half-saturation K of the neuronal capture function are not calibrated against experimental data, as direct in vivo measurements of RABV–nerve terminal binding kinetics are, to our knowledge, unavailable. These parameters are used here to explore qualitatively how switch-like versus graded capture affects neuroinvasion timing; quantitative predictions should be treated with corresponding caution until dedicated binding assays become available.

5.4 System simulation

The objective of this work was to develop an intra-host mathematical model for rabies that mechanistically integrates the main stages of viral progression, from the inoculation site to the salivary glands, and to explore the implications for post-exposure control strategies.

Table 2: Model parameters and values used for simulations.

Parameter	Description	Indicative value	Reference
Λ_m	Recruitment of healthy myocytes	10^3 cells/day	Estimated
d_m	Natural mortality of myocytes	0.01 /day	[27]
β_m	Myocyte infection rate	10^{-6} /(virion·day)	[24]
p_m	Viral production by infected myocyte	10 virions/cell/day	[27]
δ_m	Elimination of infected myocytes	0.1 /day	Estimated
ϕ_m	Immune elimination of myocytes	0.1 /(immune unit·day)	Estimated
c_v	Natural viral degradation	1 /day	[27]
ϕ_v	Immune neutralization of virus	0.05 /(immune unit·day)	Estimated
K	Half-saturation of neuronal capture	10^3 virions	Estimated†
q	Cooperativity of neuronal capture	1 or 2	Estimated†
Λ_n	Renewal of nerve endings	10^2 /day	Estimated
d_n	Natural decay of neurons	0.005 /day	Estimated
β_n	Neuronal capture rate	10^{-5} /(virion·day)	[24]
δ_n	Mortality of infected peripheral neurons	0.05 /day	Estimated
ρ	Entry into axonal transport	0.5 /day	[24]
γ_k	Axonal transition rate (each step)	0.2 /day	[10]
μ_k	Viral loss during transport	0.01 /day	Estimated
n	Number of axonal compartments	3	
δ_c	Mortality of infected CNS neurons	0.05 /day	Estimated
η	Salivary viral production	10 virions/cell/day	Estimated
δ_s	Salivary viral degradation	0.1 /day	Estimated
s	Basal source of immune response	1 immune unit/day	Estimated
α	Immune stimulation rate	0.01 /(cell·day)	Estimated
κ	Saturating effect of stimulation	10^{-3} /virion	Estimated
d_E	Natural decay of immunity	0.05 /day	Estimated

† Hypothetical: no direct in vivo measurement of RABV–nerve terminal binding kinetics is, to our knowledge, available; see limitations (Section 6).

The results obtained, both analytically and numerically, provide several insights into infection dynamics and intervention levers.

The calculation of the basic reproduction number $\mathcal{R}_0$ (equation (5)) provides a simple criterion for the establishment of a local infection in the muscle. Numerical simulations confirm the behavior predicted by stability analysis: when $\mathcal{R}_0 < 1$ (Figures 10a and 6b), the local viral load $V(t)$ and infected myocytes $I_m(t)$ decay to zero, while the immune response $E(t)$ stabilizes at its disease-free equilibrium value. Conversely, for $\mathcal{R}_0 > 1$ (Figure 10a with increased β_m), local infection becomes established and leads to progressive invasion of neuronal compartments. This threshold strongly depends on local viral replication parameters (β_m, p_m) and basal immunity (ϕ_m, ϕ_v), underscoring the importance of the innate immune response in early infection control.

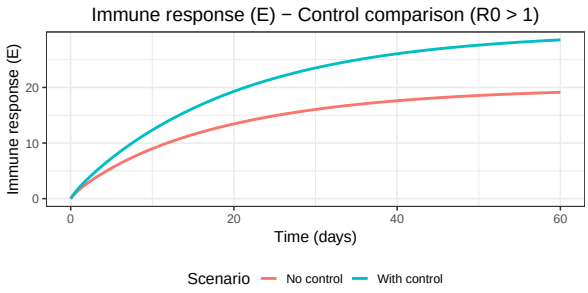
The originality of the model lies in the chain of axonal compartments representing retrograde virus transport to the central nervous system (CNS). The index $\mathcal{R}_n$ (equation (10)) was proposed as a mechanistic measure of the probability that the virus reaches the CNS, accounting for nonlinear neuronal capture, neuronal mortality, and transport losses.

Simulations show that the number of axonal compartments n does not affect the dynamics of the local viral load $V(t)$ (Figure 11) because it is coupled to the axonal chain only via the capture term, but it modifies the time of appearance of infected CNS neurons $C(t)$. For $n = 1$, CNS infection manifests rapidly after entry into peripheral neurons; for $n = 3$, a clear delay is observed, corresponding to the transit time through the three axonal steps. This property is essential because it reproduces the therapeutic window observed in post-exposure prophylaxis: the longer the delay before CNS involvement, the more effective late interventions can be.

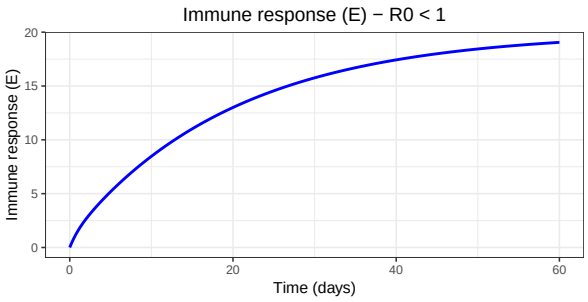
In the current formulation, n and the transition rates γ_k are treated as free parameters. Biologically, both the number of effective axonal segments and the total transit time scale with the anatomical distance d between the bite site and the CNS (e.g. distal limb vs. facial bite). A natural refinement is to fix a reference transit time $\tau(d)$ (increasing in d, consistent with the markedly shorter incubation periods observed for facial/head bites) and set $\gamma_k = n/\tau(d)$ for a fixed n, so that the total mean transit time $\sum_k 1/\gamma_k = \tau(d)$ scales with bite location while the discretization n controls the sharpness of the transit-time distribution (an Erlang-type delay). This distance-dependent calibration is left for future work pending compartment-specific transit data.

As an illustrative benchmark, we first examine the effect of applying constant controls $(u_1 = u_2 = u_3 = 0.5)$ in the scenario $\mathcal{R}_0 > 1$ (Figures 6a–10b), before comparing this benchmark against the actual optimal control obtained via the forward–backward sweep method.

As an illustrative benchmark, Figures 6a–10b show infection dynamics under a constant-effort intervention ($u_i = 0.5$ for all $t \in [0, T]$). To assess the actual performance of the proposed intervention strategy, we additionally solved the full state-adjoint optimality system (1)–(12) together with the characterizations (13)–(15) using the forward–backward sweep method described in Section 5.1, and compared the resulting optimal controls $(u_1^\star, u_2^\star, u_3^\star)$ against this constant benchmark and against the uncontrolled case, over a $T = 30$-day post-exposure horizon in the $\mathcal{R}_0 = 2.38$ regime (Figures 12–13). The optimal controls display markedly non-constant, biologically interpretable profiles: $u_1^\star$ and $u_3^\star$ are near-maximal immediately after exposure and decay to zero within approximately 2 days, consistent with immediate wound care and immunoglobulin infiltration, whereas $u_2^\star$ remains near zero during this early phase and only increases later (peaking around days 20–25), once CNS invasion has progressed and salivary dissemination becomes the

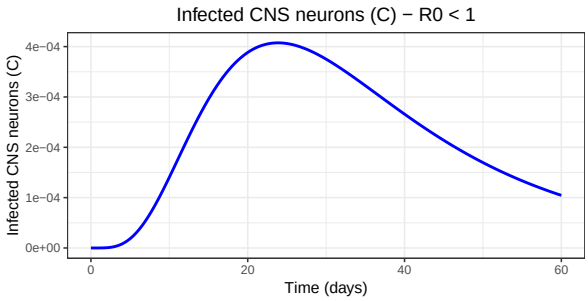


(a) Immune response $E(t)$ under constant control $u_i = 0.5$ vs. no control, in the $\mathcal{R}_0 > 1$ regime.

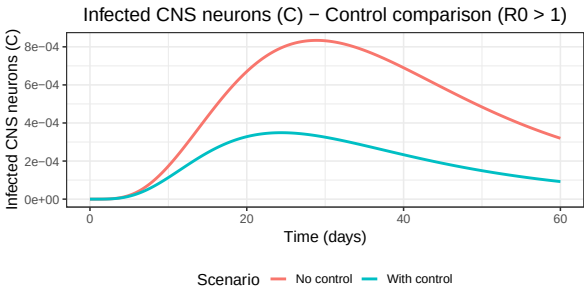


(b) Immune response $E(t)$ under the disease-free scenario $\mathcal{R}_0 < 1$, converging to $E^\star = s/d_E$.

Figure 6: Immune response $E(t)$: disease-free convergence (right) vs. constant-control benchmark in the endemic regime (left).

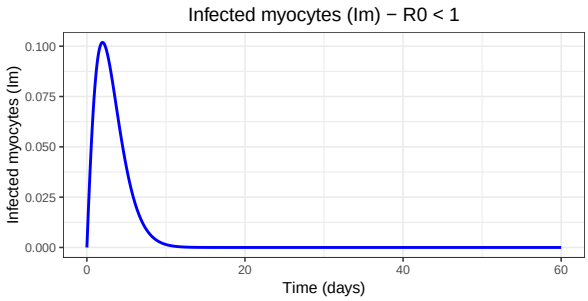


(a) Infected CNS neurons $C(t)$ under $\mathcal{R}_0 < 1$, decaying to zero as predicted by Theorem 3.6.

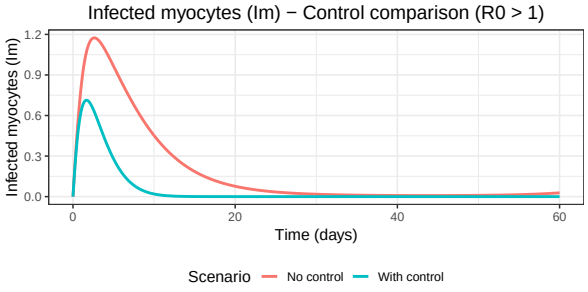


(b) Infected CNS neurons $C(t)$ under constant control $u_i = 0.5$ vs. no control, in the $\mathcal{R}_0 > 1$ regime.

Figure 7: Infected CNS neurons $C(t)$: disease-free decay (left) vs. constant-control benchmark in the endemic regime (right).

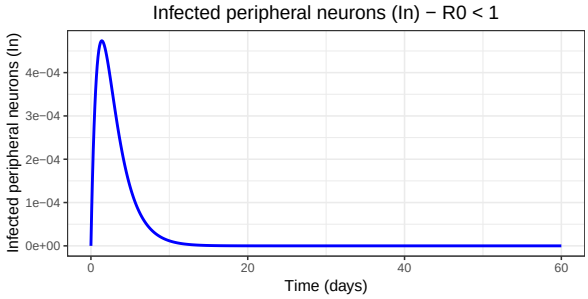


(a) Infected myocytes $I_m(t)$ under $\mathcal{R}_0 < 1$, decaying to zero.

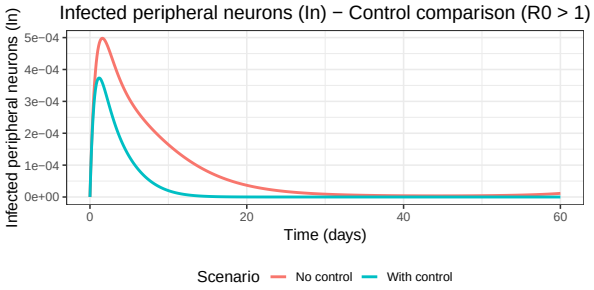


(b) Infected myocytes $I_m(t)$ under constant control $u_i = 0.5$ vs. no control, in the $\mathcal{R}_0 > 1$ regime.

Figure 8: Infected myocytes $I_m(t)$: disease-free decay (left) vs. constant-control benchmark in the endemic regime (right).

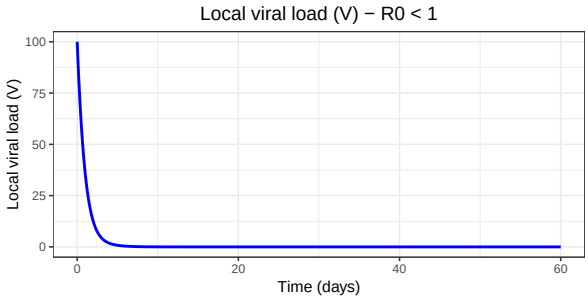


(a) Infected peripheral neuronal units $I_n(t)$ under $\mathcal{R}_0 < 1$, decaying to zero.

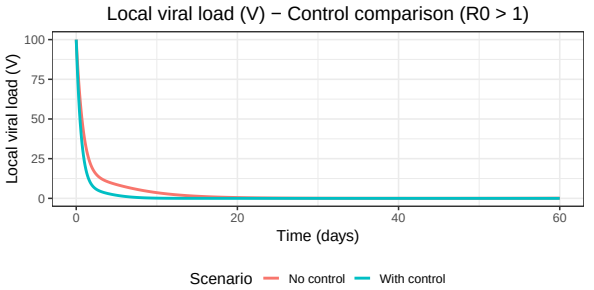


(b) Infected peripheral neuronal units $I_n(t)$ under constant control $u_i = 0.5$ vs. no control, in the $\mathcal{R}_0 > 1$ regime.

Figure 9: Infected peripheral neuronal units $I_n(t)$: disease-free decay (left) vs. constant-control benchmark in the endemic regime (right).



(a) Local viral load $V(t)$ under $\mathcal{R}_0 < 1$ (decay) and $\mathcal{R}_0 > 1$ (amplification, increased β_m), illustrating the threshold behavior of Theorem 3.6.



(b) Local viral load $V(t)$ under constant control $u_i = 0.5$ vs. no control, in the $\mathcal{R}_0 > 1$ regime.

Figure 10: Local viral load $V(t)$: disease-free/endemic threshold behavior (left) vs. constant-control benchmark in the endemic regime (right).

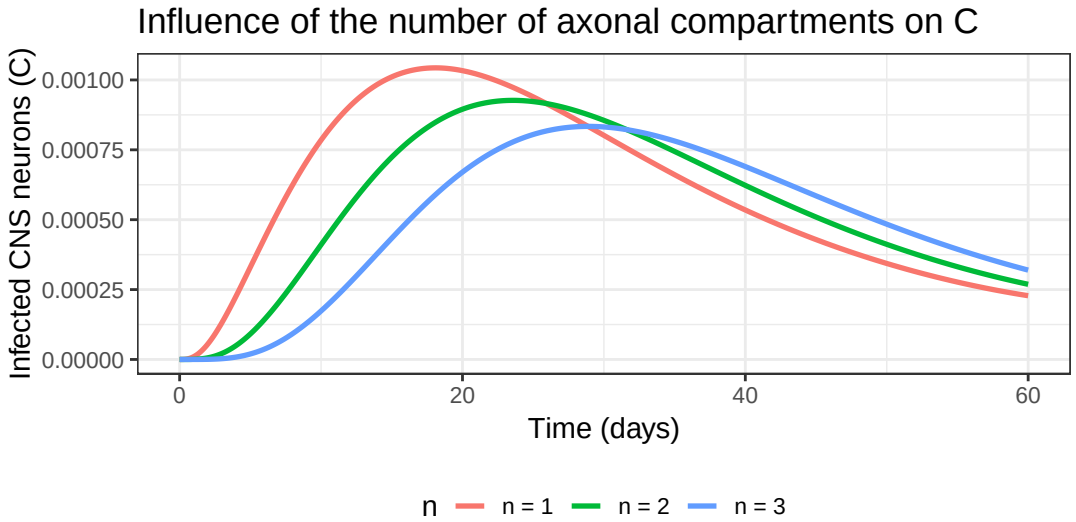


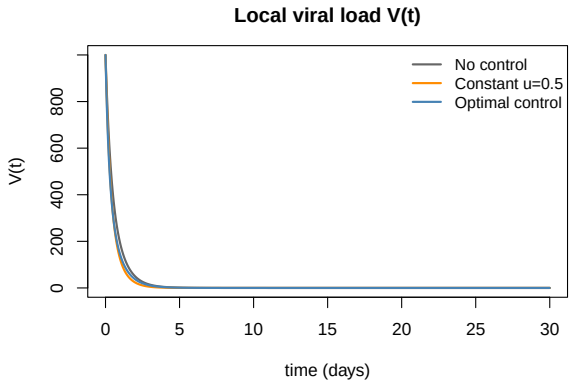
Figure 11: Influence of the number of axonal compartments $n \in \{1, 2, 3\}$ on the time course of infected CNS neurons $C(t)$: increasing n delays CNS invasion without changing the local viral dynamics $V(t)$, illustrating the therapeutic-window mechanism discussed in the text.

dominant contributor to the cost functional. This is a direct, model-derived justification for why local neutralization and immune stimulation are prioritized early while salivary-load control is comparatively less relevant in the early post-exposure window, and it emerges from the optimality conditions rather than being assumed a priori.

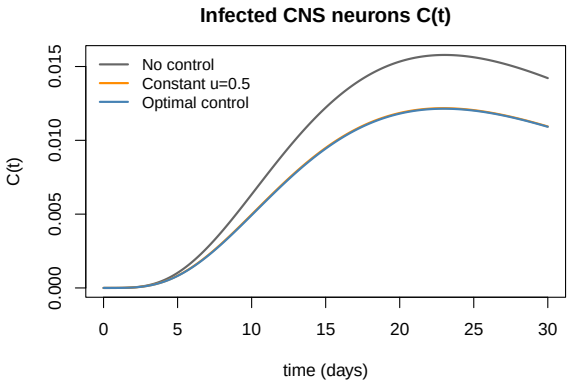
Table 3 quantifies these results: the optimal control reduces the total cost J by 83.0% relative to the constant-control benchmark $u_i = 0.5$, and by 38.6% relative to no intervention, despite using substantially less cumulative control effort. Interestingly, the constant-control benchmark achieves a lower *peak* salivary load than the optimal control ($S_{\max} = 0.201$ vs. 0.418); this reflects that $u_i = 0.5$ over-invests in salivary suppression throughout the horizon at a control cost that the optimal solution correctly identifies as not worthwhile under the chosen cost weights w_i, a_i – illustrating precisely why solving the optimality system, rather than relying on ad hoc constant controls, is necessary to identify genuinely cost-effective intervention timing.

Table 3: Comparison of no control, constant control ($u_i = 0.5$), and optimal control (forward–backward sweep), $T = 30$ days, $\mathcal{R}_0 = 2.38$.

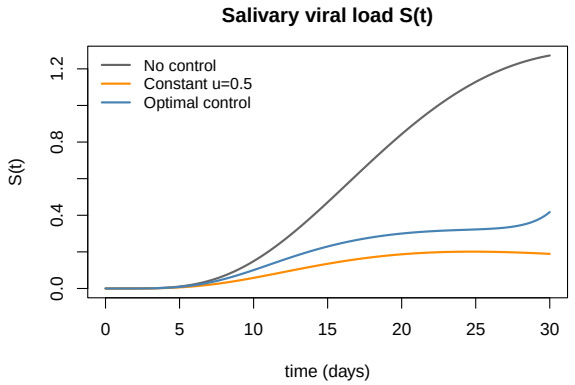
Scenario	peak V	peak C	peak S	t_{CNS} (days)	Cost J
No control	1.0×10^3	0.0158	1.270	11.21	2.252
Constant $u_i = 0.5$	1.0×10^3	0.0122	0.201	11.12	8.143
Optimal control	1.0×10^3	0.0121	0.418	11.15	**1.383**



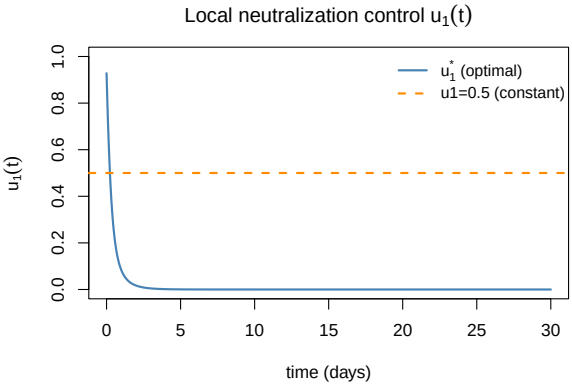
(a) Local viral load $V(t)$



(b) Infected CNS neurons $C(t)$

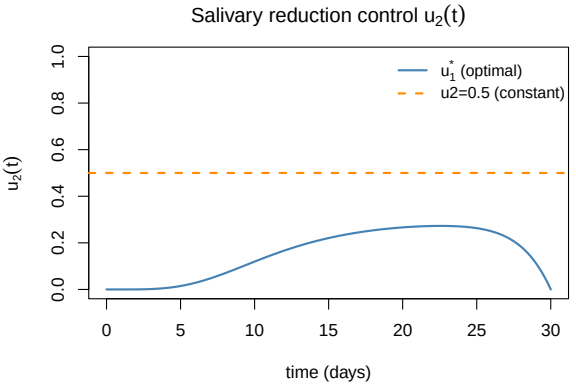


(c) Salivary viral load $S(t)$

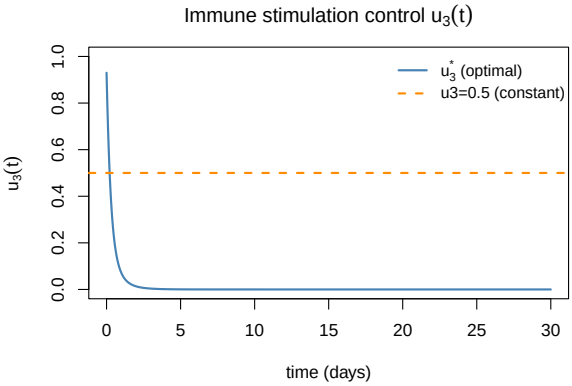


(d) Local neutralization control $u_1^\star(t)$

Figure 12: State trajectories and the first optimal control, comparing no control, constant control ($u_i = 0.5$), and the optimal control obtained via the forward–backward sweep method, over $T = 30$ days in the $\mathcal{R}_0 = 2.38$ regime. Panels (a)–(c): local viral load, infected CNS neurons, and salivary viral load under the three scenarios. Panel (d): optimal control $u_1^\star(t)$ (solid) versus the constant benchmark $u_1 = 0.5$ (dashed).



(a) Salivary reduction control $u_2^\star(t)$



(b) Immune stimulation control $u_3^\star(t)$

Figure 13: Remaining two optimal control profiles (continuation of Figure 12), each compared to the constant benchmark $u_i = 0.5$ (dashed). Panel (a): $u_2^\star(t)$ remains near zero for the first two weeks and only increases once CNS infection progresses. Panel (b): $u_3^\star(t)$, like $u_1^\star(t)$, is near-maximal immediately after exposure and decays to zero within about 2 days.

6 Limitations

We summarize here the main modeling simplifications and open extensions discussed throughout the text. The immune compartment $E(t)$ aggregates innate and adaptive responses, appropriate for the early post-exposure window (7–14 days) but not for longer timescales. The Hill parameters q and K are not calibrated against experimental data and are used for qualitative exploration only (Table 2). The axonal chain is distance-independent, with n and γ_k as free parameters; a distance-dependent calibration $\gamma_k = n/\tau(d)$ is proposed but not implemented (Section 5.3). The optimal control problem is solved in continuous time, whereas clinical prophylaxis is administered as discrete impulses; the impulsive formulation is left for future work (Section 4). The linear salivary shedding term ηC neglects saturating bottlenecks but does not affect the stability results of Section 3. A rigorous threshold for $\mathcal{R}_n$ in the regime $\mathcal{R}_0 > 1$ is not established (see Remark after Theorem 3.6). The optimal control reduces peak CNS infection by 2.5–30% depending on the initial dose, but does not meaningfully delay CNS invasion under the present parameters. Finally, the cost weights w_i, a_i were chosen for informative control trajectories rather than from clinical data, which are unavailable.

7 Conclusion

We have developed an innovative intra-host mathematical model for rabies infection, which integratively captures the key biological processes: local muscle replication, nonlinear neuronal capture, structured axonal transport in compartments, central nervous system invasion, and salivary dissemination. The axonal chain structure, combined with a Hill-type capture function, constitutes a significant advance over previous models by explicitly representing the delay and efficacy of neuroinvasion, two determining factors for the therapeutic window of post-exposure prophylaxis.

Mathematical analysis established fundamental results of positivity, boundedness, and stability – including global asymptotic stability of the disease-free equilibrium for any Hill cooperativity $q \geq 1$ – as well as a local infection threshold $\mathcal{R}_0$ and a mechanistic neuroinvasion index $\mathcal{R}_n$. These tools provide a basis for quantitatively evaluating the impact of biological parameters and interventions. The formulation of an optimal control problem, with explicit optimality conditions solved numerically via a forward–backward sweep method, demonstrates that optimally timed intervention outperforms constant-effort intervention by 83% in total cost, while revealing distinct temporal priorities for local neutralization, immune stimulation, and salivary control.

This work lays the foundations for future extensions, notably distance-dependent calibration of the axonal chain, an impulsive-control formulation matching real prophylaxis schedules, and experimental calibration of the neuronal capture and salivary shedding parameters (Section 6). Ultimately, this framework could contribute to the optimization of prophylactic protocols and to a better understanding of rabies dynamics in humans. Recent work on rabies modeling at the population level has highlighted the importance of domestic animal vaccination as a barrier against human exposure [14]. Our intra-host approach could be coupled with such population models for an integrated analysis.

8 Funding Statement

The authors received no specific funding for this research.

9 Data availability

No empirical datasets were generated or analysed during the current study. All information necessary to understand the model and its mathematical analysis is provided in the manuscript.

References

[1] Z. Ahmad, S. Ullah, M. A. Khan, and F. S. Alshammari. A fractional-order model of rabies transmission using the atangana–baleanu–caputo derivative with optimal control and cost-effectiveness analysis. *Journal of Computational and Applied Mathematics*, 5:100065, 2025.

[2] N. Ahmed, A. Elhassanein, and F. A. Rihan. Computationally efficient optimal control analysis for the mathematical model of coronavirus pandemic. *Expert Systems With Applications*, 234:121094, 2023.

[3] N. Ahmed, F. A. Rihan, and M. R. Alharthi. Analytical and numerical studies of optimal control techniques for ebola virus disease management. *European Physical Journal Plus*, 140(4):329, 2025.

[4] Muhammad Aslam et al. Analytical and numerical boundedness of a model with memory effects for the spreading of infectious diseases. *Symmetry*, 14(12):2540, 2022.

[5] A. Berliner et al. Optimal post-exposure vaccination strategies for rabies. *Journal of Theoretical Biology*, 450:1–12, 2018.

[6] Mfano Charles, Sayoki G. Mfinanga, G. A. Lyakurwa, Delfim F. M. Torres, and Verdiana G. Masanja. A mathematical and optimal control model for rabies transmission dynamics among humans and dogs with environmental effects. *Journal of Applied Mathematics*, 2025, 2025.

[7] D. Colombi, C. Poletto, E. Nakoune, H. Bourhy, and V. Colizza. Long-range movements coupled with heterogeneous incubation period sustain dog rabies at the national scale in africa. *PLoS Neglected Tropical Diseases*, 2020.

[8] Amr Elsonbaty and A. El-Mesady. Fractional-order model for two-strain monkeypox virus: Analytical and numerical insights with optimal control strategies. *Partial Differential Equations in Applied Mathematics*, 14:101229, 2025.

[9] Wendell H. Fleming and Raymond W. Rishel. *Deterministic and Stochastic Optimal Control*. Springer-Verlag, 1975.

[10] A. R. Fooks, P. N. Johnson, and H. Rupprecht. Rabies virus pathogenesis and the post-exposure prophylaxis. *Clinical Microbiology Reviews*, 16(3):413–440, 2003.

[11] Shani Gluska, Eitan Erez Zahavi, Michael Chein, Tal Gradus, Anja Bauer, Stefan Finke, and Eran Perlson. Rabies virus hijacks and accelerates the p75ntr retrograde axonal transport machinery. *PLoS Pathogens*, 10(8):e1004348, 2014.

[12] Nathan J. Hardenbrook and William Wan. Using cryo-electron tomography to study the molecular mechanisms of neurotropic viral infections using rabies as a model system. *Microscopy and Microanalysis*, 31(Supplement_1), 2025.

[13] Philip Hartman. *Ordinary Differential Equations*. SIAM, 2002.

[14] Annalise Hassan et al. Mathematical model of rabies vaccination in the united states. *Theoretical Population Biology*, 2024.

[15] A. V. Hill. The possible effects of the aggregation of the molecules of haemoglobin on its dissociation curves. *Journal of Physiology*, 40(suppl):iv–vii, 1910.

[16] M. Iqbal, N. Ahmed, and M. Ali. Modeling rabies evolution with vaccination: A fractional calculus perspective. *Informatics in Medicine Unlocked*, 30:e03001, 2025.

[17] M. A. Khan, F. S. Alshammari, and S. Ullah. Optimal control and cost-effectiveness analysis of bovine tuberculosis transmission dynamics. *Parasite Epidemiology and Control*, 27:e00287, 2024.

[18] M. A. Khan, E. O. Alzahrani, and F. A. Rihan. Dynamics of bi-susceptibility patterns in COVID-19 epidemics and associated abstinence strategies. *Modeling Earth Systems and Environment*, 11:198, 2025.

[19] M. A. Khan, S. Ullah, and M. Farooq. A fractional-order model for rabies transmission dynamics using the atangana–baleanu–caputo derivative and MCMC methods. *Scientific African*, 29:e02800, 2025.

[20] Joseph P LaSalle. Some extensions of liapunov's second method. *IRE Transactions on Circuit Theory*, 7(4):520–527, 1960.

[21] Suzanne Lenhart and John T. Workman. *Optimal Control Applied to Biological Models*. Chapman and Hall/CRC, 2007.

[22] Suzanne Lenhart and John T. Workman. *Optimal Control Applied to Biological Models*. Chapman & Hall/CRC, 2007.

[23] T. L. Lentz. Neural mechanisms of rabies virus transport. *Progress in Neurobiology*, 18(3):263–280, 1982.

[24] Y. Liu and J. Zhou. Mathematical model for rabies virus transport along neurons. *Mathematical Biosciences*, 226(2):119–128, 2010.

[25] C. Mao, D. E. Cahill, and M. A. Dietz. Spread of rabies virus within the central nervous system. *Journal of Virology*, 70(6):3764–3771, 1996.

[26] M. A. Nowak and R. M. May. *Virus dynamics: mathematical principles of immunology and virology*. Oxford University Press, Oxford, UK, 2000.

[27] A. S. Perelson. Modelling viral and immune system dynamics. *Nature Reviews Immunology*, 2(1):28–36, 2002.

[28] Lev S. Pontryagin, Vladimir G. Boltyanskii, Revaz V. Gamkrelidze, and Evgenii F. Mishchenko. *The Mathematical Theory of Optimal Processes*. Interscience Publishers, 1962.

[29] F. A. Rihan, G. Velmurugan, and F. S. Alshammari. Modeling the impact of optimized treatment regimens on dengue transmission dynamics. *Chaos: An Interdisciplinary Journal of Nonlinear Science*, 35(10), 2025.

[30] S. Y. Tchoumi, F. A. Rihan, and J. M. Tchuenche. Study of the role of antimalarial treatment and bed nets in malaria transmission and control by mathematical modeling. *Computer Modeling in Engineering and Sciences*, 144(3):3463–3492, 2025.

[31] Pauline van den Driessche and James Watmough. Reproduction numbers and subthreshold endemic equilibria for compartmental models of disease transmission. *Mathematical biosciences*, 180(1-2):29–48, 2002.

[32] Marya Zainab et al. Study of fractional order rabies transmission model via atangana-baleanu derivative. *Scientific Reports*, 14:25875, 2024.

[33] L. Zhang and H. Li. Modeling post-exposure rabies vaccination with control theory. *Applied Mathematics and Computation*, 357:273–284, 2019.